

**Title: Unlocking peroxide activation initiated by a solid-water interface**

**Authors:** Wan-Ting Li<sup>1,3†</sup>, Jian-Hua Chen<sup>1†</sup>, Kun-Yu Cai<sup>1</sup>, Hui-Jie Tu<sup>1,2</sup>, Shoaib Akhtar<sup>1</sup>, Lin-Dong Liu<sup>1,2,3\*</sup>

**Affiliations:**

<sup>1</sup>Laboratory of Environmental Interface and Water Pollution Control, College of Resources and Environment, Southwest University, Chongqing 400716, China

<sup>2</sup>Yibin Academy of Southwest University, Sichuan 644005, China

<sup>3</sup>College of Sericulture, Textile and Biomass Sciences, Southwest University, Chongqing 400716, China

\*Corresponding author. Email: [lindongliu@swu.edu.cn](mailto:lindongliu@swu.edu.cn)

†These authors contributed equally to this work.

**Abstract:**

Activation of the peroxide (O–O) bond at a solid-liquid interface is a key aspect of biological and chemical oxidation reactions due to its fundamental role. An oxidation mechanism exemplified by typical Fenton-like persulfate-based heterogeneous oxidation, in which electron transfer dominates, is almost universally accepted. However, we present experimental results that challenge this view. At a solid-liquid interface, we show that protons are thermodynamically coupled to electrons. *In situ* quantitative titration yielded direct experimental evidence that the coupling ratio of protons to transferred electrons was 1:1, indicating a net proton-coupled electron transfer in which both the proton and electron enter the redox cycle. These findings will inform future developments in peroxide activation technologies, enabling more efficient redox activity via tight coupling of protons and electrons.

**One-Sentence Summary:**

At a solid-water interface, activation of the persulfate O–O bond actually occurs by the coupled transport of both proton and electron equivalents rather than by pure electron transfer.

**Main Text:**

Transition metal-mediated O–O bond activation plays pivotal roles in many biological and chemical oxidation reactions, which are particularly important for sustainable solutions to the problems currently faced by modern society (1–10). Chemical oxidation using metal oxide materials ( $\text{MO}_x$ ) at solid-solution interfaces [e.g., redox processes used for sustainable water treatment (2,11)] are typically described using the redox paradigm. However, the electron transfer (ET)–centered view of redox reactions is increasingly challenged in the context of reaction thermochemistry (12–14) because chemical bonds are formed or broken via the temporary addition or removal of electrons. In such instances, an electron may be transferred in conjunction with a proton, through a mechanism termed proton-coupled electron transfer (PCET) (15,16). This interdependent coupling occurs when the free energy perturbations associated with ET at the interface of a redox system cannot be disregarded (12,17,18). The coupling implies that the initial and final states of ET significantly differ because of non-zero nuclear reorganization (i.e., solvent reorganization and/or ion transfer). Here, we focus on charge-compensated cation coupling, in which the free energy of ET reflects the characteristics of the cations, rather than the intrinsic properties of  $\text{MO}_x$ . This coupling ensures that thermodynamic equilibrium is reached, thereby implying that PCET is thermodynamically preferred. However, such joint participation of electrons and protons conflicts with the prevailing view of an interfacial redox reaction, in which the fundamental nature of the reaction is regarded as the addition or removal of electrons (i.e., pure ET). Despite extensive research regarding redox bond-making/breaking at solid-solution interfaces (19–21), there remains a lack of knowledge concerning the coupled proton transfer (PT) and ET of redox processes used for sustainable water treatment (2,11); this lack of knowledge hinders improvement. This study explicitly demonstrates that proton coupling at a solid-solution interface typically accompanies ET, stimulating further investigation of how redox water treatments could be improved.

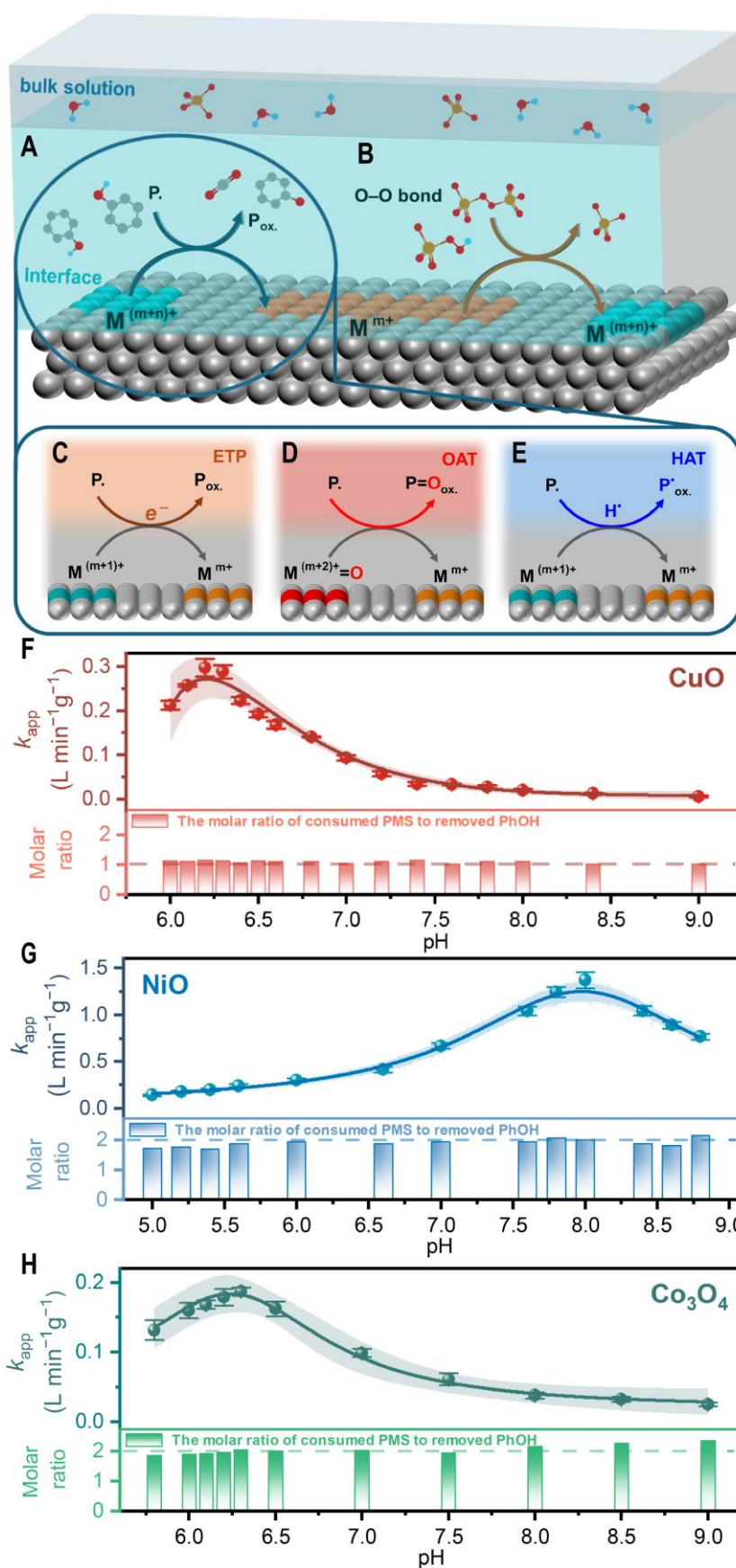


**Fig. 1. Two interlinked redox half-reactions, three currently recognized oxidation pathways, and the experimentally validated non-monotonic kinetics-pH dependencies. Activation of the**

O–O bond at a solid-water interface is initiated by two interlinked redox half-reactions. The first, termed **(A)**, is the transition from  $M^{(m+n)+}$  [high-valent metal (–oxo) species] to  $M^{m+}$  (low-valence metal), which serves as a key process in the oxidation of model pollutants. The second is **(B)**, the transition from  $M^{m+}$  to  $M^{(m+n)+}$ , which involves cleavage of the O–O bond. The conventional categorization of oxidation pathways as **(C)** ETP and **(D)** OAT, which focuses primarily on electron transfer, is inadequate because it does not include the formation of high-valent metal (–oxo) species. The **(E)** HAT hypothesis is untenable because it assumes that the proton and electron originate and terminate in the same bond. In the case of transition metal-mediated O–O bond activation at a solid-water interface, the electron ( $e^-$ ) is typically found occupying the available  $d$ -state at the metal site, while the proton ( $H^+$ ) attaches to the interfacial O atom. The volcano plot of the apparent rate constant ( $k_{app}$  in  $L\ min^{-1}\ g^{-1}$ ) versus pH and the molar ratio of consumed PMS to removed PhOH for **(F)** CuO, **(G)** NiO, and **(H)**  $Co_3O_4$  is shown here for mean values and error bars. Error bars indicate the standard deviation of duplicate measurements ( $n = 2$ ). Experimental conditions: [PMS] = 0.3 mM, [PhOH] = 0.15 mM, catalyst = 0.2 g  $L^{-1}$ ,  $T = 25 \pm 2\ ^\circ C$ , 0.2 M borate or glycine buffer. P., model pollutants;  $P_{ox.}$ , oxidation products;  $P=O_{ox.}$ , oxygen atom transfer products;  $P^*_{ox.}$ , hydrogen atom transfer products.

Persulfate-based heterogeneous oxidation is a prototypical and extensively studied redox wastewater treatment process (22–25) (Fig. S1). In the present study, we study this well-defined Fenton-like reaction system, which ensures water safety. Benchmark  $MO_x$ -based catalysts activate the O–O bonds of persulfate precursors—peroxymonosulfate (PMS,  $HO-OSO_3^-$ ) and peroxydisulfate (PDS,  $O_3SO-OSO_3^{2-}$ ) (Fig. S2)—enabling the linkage of  $MO_x$  metal redox transformation to the oxidation of organic pollutants. The process can be subdivided into high-valent, metal-induced, non-radical oxidation steps (Figs. 1A and 1B). This process has created a paradigm shift in the water treatment field; the historical focus on pollution control has shifted toward a more sustainable approach that incorporates resource recovery (26,27). This shift changed the mode of organic elimination from mineralization (associated with production of  $CO_2$  and  $H_2O$ ) to polymerization, enabling water purification to be associated with low-level carbon emissions (2,3,28). Using this knowledge, significant advances have been made in the development of sustainable water treatments (2,3,28). However, the high-valent, metal-induced, oxidation mechanism remains unclear; there are three currently recognized oxidation pathways (29): An electron-transfer process (ETP), hydrogen atom transfer (HAT), and oxygen atom transfer (OAT) (Figs. 1C–E). All primarily involve redox-driven ET; the coupled protons have been largely

overlooked. We hypothesize that PT, similar to ET, occurs at a solid-water interface.

The present study examines the proton-coupled nature of well-characterized interfacial redox reactions, with a particular focus on persulfate-based heterogeneous oxidation. The volcano relationship between the rate constant and the pH, exemplified by one benchmark  $\text{MO}_x$ -based catalyst ( $\text{CuO}$ ), is confirmed. Mechanistic studies indicate that activation of the persulfate O–O bond is only mediated by interfacial Cu sites *via* a concerted PCET (CPET) pathway, yielding high-valent metal (–oxo) species ( $\text{Cu}^{\text{III}}$ ) that serve as key intermediates during the oxidation of model pollutants including phenol (PhOH) and 2,6-dimethylphenol (2,6-M-PhOH) to organic radicals. Thus, both processes facilitate radical polymerization at a solid-water interface. The catalytic activity during oxidative polymerization is affected by the proton activity (pH); pH significantly alters the activity (up to 46.33-fold for  $\text{Cu}^{\text{III}}$ ). Quantitative acid–base titrations tracking the evolution of  $[\text{H}^+]$  reveal that, during CPET, the  $\text{H}^+/\text{e}^-$  stoichiometry is almost 1:1. Changes in pH affect the CPET process of other benchmark  $\text{MO}_x$  ( $\text{NiO}$  and  $\text{Co}_3\text{O}_4$ ) and thus the oxidation activities of  $\text{Ni}^{\text{IV}}=\text{O}$  and  $\text{Co}^{\text{IV}}=\text{O}$ . Oxidative polymerization can be extended to another typical aromatic, aniline, yielding organic polymers; these results demonstrate the generalizability of CPET in terms of initiating radical polymerization at a solid-water interface.

### ***Mechanisms solely focused on ET do not explain the non-monotonic kinetic/pH dependencies***

Our study began with pH activity profiling (Figs. 1F–H) in a batch reactor with representative reactants: benchmark  $\text{MO}_x$  ( $\text{CuO}$ ,  $\text{NiO}$ , and  $\text{Co}_3\text{O}_4$ ) (30), a persulfate oxidant, and model pollutants. The studied pH range is detailed in Note S1. The catalytic activity of the model  $\text{CuO}$ -activated PMS process (Fig. S3) expressed as an apparent rate constant ( $k_{\text{app}}$  in  $\text{L min}^{-1} \text{g}^{-1}$ ) (Fig. S4) is not pH-dependent (PCET predicted either a volcanic or caldera-shaped kinetic dependence on pH) (14,31–33); a similar result has been previously reported (34) (Note S2). We hypothesized that the discrepancy could be resolved by considering the instantaneous change in interfacial

proton concentration (35) triggered by a reaction-induced local pH shift. One potential solution might utilize borate and glycine buffers, which attenuate the nearly interfacial local pH gradient within acceptable tolerances (Note S3). A novel finding emerged under well-buffered conditions: a large kinetic pH effect manifested as a kinetic gap of approximately two orders of magnitude (46.33-fold) (Figs. 1F, S5 and Table S1). Critically, a failure to consider the interfacial and bulk solution pH gradients can mask identification of this effect, leading to the commonly observed weak rate-pH scaling effect (Note S4). Another potentially counterintuitive result was the non-monotonic nature of the pH-dependent kinetics; the maximum  $k_{app}$  occurred at a unique inflection point of pH 6.2 (Figs. 1F, S5 and Table S1). The volcano-shaped activity versus pH profiles of other benchmark catalysts, including NiO and Co<sub>3</sub>O<sub>4</sub> (Figs. 1G, 1H, S6, S7 and Table S1), provide further evidence to support this conclusion. These profiles show that the pH-dependent activity variations described above are common. Such pH-determined behavior indicates proton activity at the solid-water interface. This proton activity has not yet been considered by researchers focused on typical interfacial redox reactions, such as persulfate-based oxidations. The non-monotonic kinetic/pH dependencies cannot be fully explained by the conventional ET-focused view; it is essential to consider PCET.

### ***Unnoticed PT at a solid-water interface***

To identify previously unrecognized protons, we used electron equivalents that could resolve the reaction path. Electron conservation is not consistent with the conventional radical-oxidation/pollutant-mineralization mechanism (Fig. 1F, Table S2 and Note S5) (11,36); non-radical oxidation is also involved, as indicated by the near-unity molar ratio of consumed PMS to removed phenol as the pH increases from 6.0 to 9.0 when CuO is utilized (Fig. 1F). This phenomenon was expected (26). However, the relative importance of the radical and non-radical paths remains unclear. Chemical oxygen demand (COD) measurements and thermogravimetric analysis (TGA) revealed that non-radical oxidation explained > 81.51% of PhOH removal (see Methods S1–3,



and Fig. S8). Semi-quantitative electron paramagnetic resonance (EPR) studies and radical-probing experiments [using benzoic acid (37,38) and iopromide (39) to probe for  $\cdot\text{OH}/\text{SO}_4^{\cdot-}$  and  $\text{SO}_4^{\cdot-}$ , respectively] (Methods S4 and Figs. S9, S10) showed that  $\cdot\text{OH}$ ,  $\text{SO}_4^{\cdot-}$ ,  $\text{O}_2^{\cdot-}$ , and  $^1\text{O}_2$ —in either the bulk solution or surface-bound form—were not engaged in oxidation. Radicals explained less than 19.12% of PhOH oxidation (Note S6); the non-radical pathway is the primary mechanism, rather than a supporting mechanism.

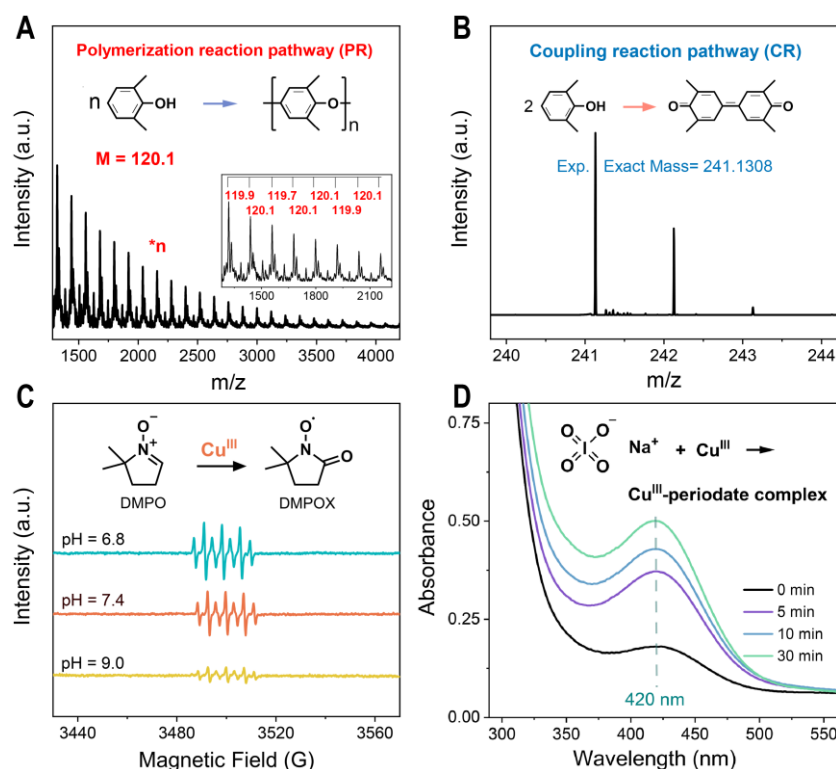


**Fig. 2. Deciphering the phenoxy radical ( $\text{PhO}\cdot$ ) intermediate of PhOH oxidation and elucidating the crucial decontamination contribution of in situ formed  $\text{Cu}^{\text{III}}$ .** (A) The MALDI-TOF-MS spectrum of the oxidation products of 2,6-M-PhOH washed with toluene. The inset in A is a partially magnified view of the MALDI-TOF-MS spectrum. It can be seen that the mean mass interval of 120.1 corresponds to the polymeric unit of poly(2,6-dimethyl-1,4-phenylene oxide) (PPO), as well as a schematic of the polymerization reaction pathway. (B) The high-resolution mass spectrum of the oxidation products of 2,6-M-PhOH washed with ethanol. The exact theoretical mass of 3,3',5,5'-tetramethyldiphenylquinone (positive ion acquisition mode,  $+\text{H}$ ) is 241.1228, which agrees with the experimental value in B (i.e. 241.1308). The inset in B shows a schematic of the surface coupling reaction pathway. The results from A and B indicate that the predominant formation is of the  $\text{PhO}\cdot$  intermediate. (C) EPR spectra of the  $\text{CuO}/\text{PMS}$  system at pH 6.8, 7.4, and 9.0 with 0.1-M DMPO as a spin-trapping agent. The positive correlation between the EPR peak height and the kinetic activity indicates that the pH-dependent production of  $\text{Cu}^{\text{III}}$  occurs. (D) Absorbance spectra of the  $\text{Cu}^{\text{III}}$ -periodate complex at 420 nm over time (0, 5, 10, 30 min). Experimental conditions:  $[\text{PMS}] = 0.3 \text{ mM}$ ,  $[\text{CuO}] = 0.2 \text{ g L}^{-1}$ ,  $T = 25 \pm 2^\circ\text{C}$ , 0.2 M borate buffer.

(D) The ultraviolet-visible spectrum of the Cu<sup>III</sup>-periodate complex showed a distinct light absorption at 420 nm, indicating the formation of Cu<sup>III</sup>. Experimental conditions: [NaIO<sub>4</sub>] = 0.5 mM, [PhOH] = 0.15 mM, [PMS] = 0.3 mM, [CuO] = 0.2 g L<sup>-1</sup>, T = 25 ± 2 °C, pH = 7.4, 0.2 M borate buffer.

Next, we explored the intermediates and products of the non-radical pathway. The surface-accumulated PhOH oxidation product was a crosslinked polymer (Fig. S8) that did not peel from the surface into the solvent (Note S7). We inferred that a reactive phenoxy radical (PhO·) intermediate (not yet directly detected) explains formation of the crosslinked polymer (Note S8), considering that PhOH exhibits three active H-sites (at the *ortho*-/*para*-positions of phenolic-OH). If this inference is correct, concealment of two-thirds of the H-sites (at the two *ortho*-positions) might hinder crosslinking. We thus implemented a hypothesis-driven approach; we modified PhOH to 2,6-M-PhOH (with only one active H-site in the *para*-position). As expected, 91.06% of 2,6-M-PhOH was converted into non-crosslinked products (Methods S5–7, and Fig. S11). Specifically, 33.82% of products were chain-like polyphenyl ethers (formed *via* C–O polymerization) (Figs. 2A and S12), whereas 57.24% of products were 3,3',5,5'-tetramethyldiphenoquinone (created *via* C–C coupling) (Fig. 2B and S13); all products formed *via* oxidation of 2,6-M-PhOH. The polymerization and coupling products were identified using COD measurements, TGA, matrix-assisted laser desorption/ionization time-of-flight mass spectrometry (MALDI-TOF-MS), gel permeation chromatography (GPC), and liquid chromatography-mass spectrometry (LC-MS) (Figs. 2A, 2B, S12–S14 and Note S9). The predominant PhO· intermediate (> 91.06%) is similar to those previously reported (2,26). Importantly, the oxidation of PhOH to yield PhO· involves a PT (40,41); this aspect cannot be disregarded.

We next sought to identify the active site for conversion of PhOH to PhO·. This site engages in selective oxidation of primary organic pollutants; the removal efficiencies differ between electron-rich (with electron-donating groups, -OH and/or -NH<sub>2</sub>) and electron-deficient (with electron-withdrawing groups, -COOH and/or -NO<sub>2</sub>) organics (Fig. S15). Moreover, the photoluminescence spectra resemble volcanoes (Fig. S16), suggesting that Cu<sup>III</sup> is the critical intermediate initiating PhO· generation. This



suggestion is supported by previous results (25) and our EPR spectra (Fig. 3C) that revealed the typical seven-line EPR signal of 5,5-dimethyl-1-pyrrolidone-N-oxyl (DMPOX) was produced *via* oxidation of 5,5-dimethyl-1-pyrroline N-oxide (DMPO) by  $\text{Cu}^{\text{III}}$ . The formation of DMPOX entails the exclusion of  $^1\text{O}_2$  and abrupt generation of a substantial quantity of  $\cdot\text{OH}$ , as described in Figure S9 and Note S10. The pronounced pH-dependent correlation between kinetic activity (Fig. S5) and EPR peak height (Fig. 3C) indicates that low-valent  $\text{Cu}^{\text{II}}$  undergoes oxidation to high-valent  $\text{Cu}^{\text{III}}$  in a pH-dependent manner. A similar conclusion can be drawn regarding the final oxidation products of methyl phenyl sulfoxide (PMSO); these are biphenyl compounds or hydroxylated products, as revealed by spectrally matched LC-MS (Fig. S17), and they were previously suspected to result from direct  $\text{Cu}^{\text{III}}$  oxidation (25). Ultraviolet–visible spectral analysis revealed a transient  $\text{Cu}^{\text{III}}$ –periodate complex (42,43) (Fig. 3D and Note S11), providing additional evidence to support our conclusion. Next, we conducted open-circuit potential versus time (OCPT) tests (Method S8 and Fig. S18) to track the efficiency of the  $\text{Cu}^{\text{III}}$ -to- $\text{Cu}^{\text{II}}$  transition with and without PhOH. Prior to PhOH addition, the dominant valence state was that of electrochemically generated  $\text{Cu}^{\text{III}}$ . However, the accelerated  $\text{Cu}^{\text{III}}$  quenching upon addition of PhOH indicated that  $\text{Cu}^{\text{III}}$  produced  $\text{PhO}\cdot$  through oxidation of PhOH. The key role of  $\text{Cu}^{\text{III}}$  was substantiated by addition of a  $\text{Cu}^{\text{III}}$  quencher (Fig. S19), after which phenol polymerization ceased. Thus,  $\text{PhO}\cdot$  production reflects oxidation by  $\text{Cu}^{\text{III}}$ .

Evaluations of other benchmark  $\text{MO}_x$ , thus  $\text{NiO}$  and  $\text{Co}_3\text{O}_4$ , revealed that high-valence  $\text{Ni}^{\text{IV}}=\text{O}$  and  $\text{Co}^{\text{IV}}=\text{O}$  were kinetically competent oxidants, associated with 97.35% ( $\text{Ni}^{\text{IV}}=\text{O}$ ) and 91.83% ( $\text{Co}^{\text{IV}}=\text{O}$ ) PhOH oxidation to  $\text{PhO}\cdot$ . The details are presented in Figures 1G, 1H, and S20. These results are comparable to the approximately 100% PhOH-to- $\text{PhO}\cdot$  reactions catalyzed by transition metal (Cu, Ni, Co, and Fe) single-atom catalysts (2). Our experiments show that high-valent metal (–oxo) species ( $\text{Cu}^{\text{III}}$ ,  $\text{Ni}^{\text{IV}}=\text{O}$ , and  $\text{Co}^{\text{IV}}=\text{O}$ ) are key intermediates of PhOH coupling/polymerization; they extract an H-atom ( $\text{H}\cdot$ ) from PhOH to generate  $\text{PhO}\cdot$  (Eqs. 1 and 2). Furthermore, our research platform enabled investigation of how

high-valent metal (–oxo) species engage in interfacial PCET (I-PCET), facilitating a deeper understanding of the I-PCET mechanism.

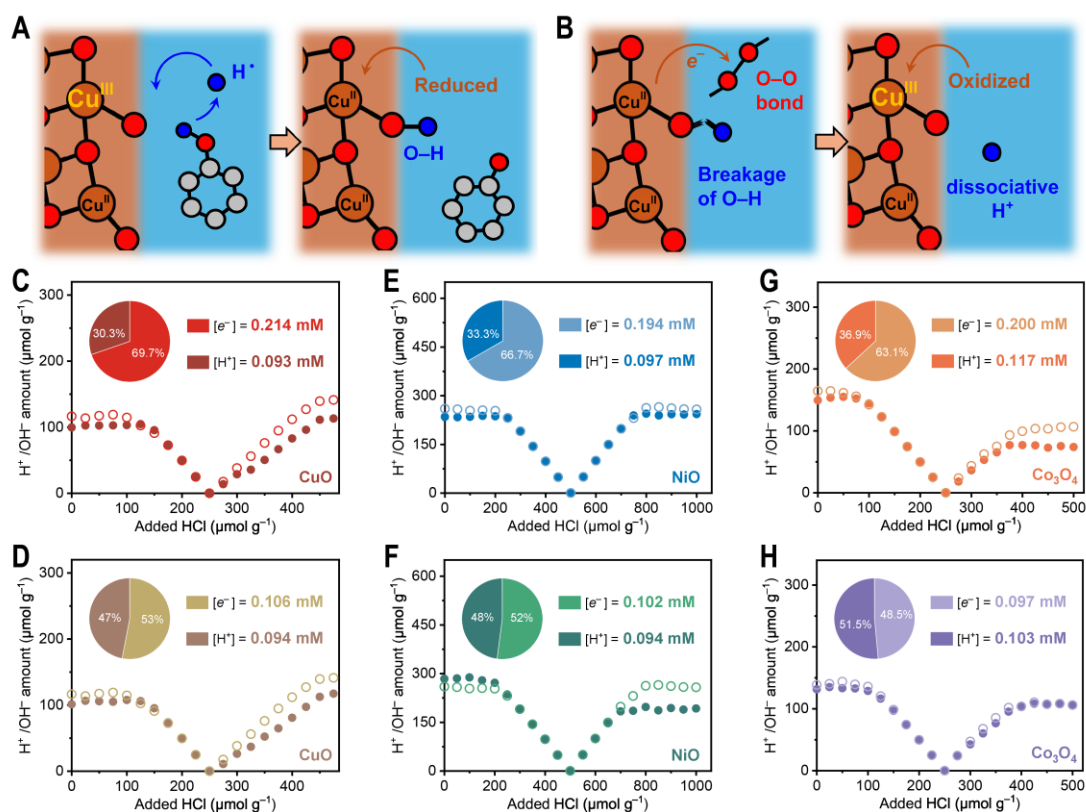
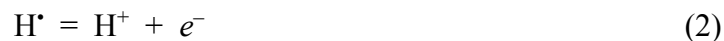
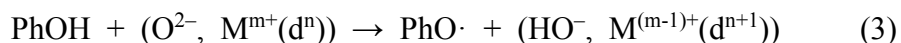


**Fig. 3. Evidence for the CPET mechanism controlling the activation of the O–O bond initiated by a solid-water interface.** A comprehensive CPET mechanism consists of two coupled redox half-reactions. The first reaction (A) is the oxidation of PhOH to PhO•, which involves the abstraction of H• from PhOH by the electrophilic Cu<sup>III</sup>, accompanied by the reduction of Cu<sup>III</sup> to Cu<sup>II</sup>. In contrast, the latter (B) is characterized by the formation of Cu<sup>III</sup> from Cu<sup>II</sup> through heterolytic O–O bond activation, where the molar ratio of transferred electrons to coupled protons is close to 1:1, as shown in this study. This indicates that the interfacial O–H bond is directly involved in the oxidation of Cu<sup>II</sup> to Cu<sup>III</sup>. This suggests that the O–H bond is simultaneously broken in response to the temporary removal of an electron from Cu<sup>II</sup> to Cu<sup>III</sup>. This, in turn, suggests that the conversion of Cu<sup>III</sup> to Cu<sup>II</sup> corresponds to the formation of O–H bonds, as shown in A. The capture and quantification of the coupled protons were achieved by the implementation of an appropriately performed liquid-phase acid–base titration for (C) CuO/PMS (experimental conditions: [PMS] = 0.1 mM, [CuO] = 2.0 g L<sup>−1</sup>), (D) CuO/PDS (conditions: [PDS] = 0.1 mM, [CuO] = 2.0 g L<sup>−1</sup>), (E) NiO/PMS (conditions: [PMS] = 0.1 mM, [NiO] = 2.0 g L<sup>−1</sup>), (F) NiO/PDS (conditions: [PDS] = 0.1 mM, [NiO] = 2.0 g L<sup>−1</sup>), (G) Co<sub>3</sub>O<sub>4</sub>/PMS (conditions: [PMS] = 0.01 mM, [Co<sub>3</sub>O<sub>4</sub>] = 4.0 g L<sup>−1</sup>), and (H) Co<sub>3</sub>O<sub>4</sub>/PDS (conditions: [PDS] = 0.1 mM, [Co<sub>3</sub>O<sub>4</sub>] = 2.0 g L<sup>−1</sup>). The molar ratio of coupled protons to transferred electrons, as determined by titration, is 1:2 for C, E, and G, while the ratio is 1:1 for D, F, and H.

These results indicate that the formation of the high-valent metal (–oxo) species is significantly influenced by the stoichiometric proton/electron coupling ratio.

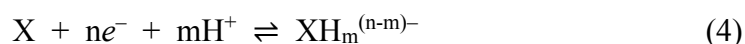
### *Evidence for I-PCET*

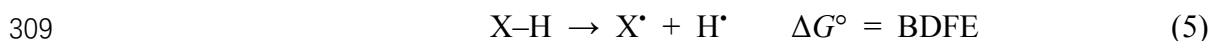
Two general mechanisms, hydrogen atom transfer (HAT) and CPET (2), involve extraction of H<sup>•</sup> from PhOH by electrophilic high-valent metal (–oxo) species (Cu<sup>III</sup>, Ni<sup>IV</sup>=O, and Co<sup>IV</sup>=O). The low kinetic isotope effect of *k* [KIE, KIE = *k*<sub>PhOH(H)</sub>/*k*<sub>PDOD(D)</sub>] (Method S9 and Fig. S21) and its high temperature dependence [i.e., KIE inversion at higher temperatures (32)] (Fig. S22), show that CPET is involved. Thus, the proton (H<sup>+</sup>) and electron (e<sup>−</sup>) respectively originate and terminate the distinct bonds. In contrast, HAT requires H<sup>+</sup> and e<sup>−</sup> to both originate and terminate the same bonds (44). In the context of benchmark transition metal oxides (CuO, NiO, and Co<sub>3</sub>O<sub>4</sub>), CPET is plausible considering that e<sup>−</sup> populates the available *d* states of the metal and H<sup>+</sup> attaches to the interfacial O atom (Eq. 3). These observations indicate that oxidation of PhOH to PhO<sup>•</sup> is a form of coupled H<sup>+</sup>/e<sup>−</sup> transfer (1:1 H<sup>+</sup>:e<sup>−</sup> stoichiometry), followed by CPET-mediated H<sup>+</sup>/e<sup>−</sup> addition to distinct interfacial trapping sites (Fig. 3A). Thus, the high-energy intermediates typically observed during sequential ET and PT steps are absent. The negligible variation in solution pH after high-valent metal (–oxo) species react with PhOH reinforces this conclusion (Fig. S23). Notably, the PCET mechanism involved at a solid-water interface is composed of two interlinked redox half-reactions. The initial reaction is substrate oxidation; a high-valent metal (–oxo) species is the active oxidant (described above) (Figs. 1A and 3A). The second reaction comprises formation of a high-valent metal (–oxo) species *via* heterolytic O–O bond activation (12) (Fig. 1B). Nevertheless, an understanding of the I-PCET process is compromised by the limited data regarding the coupled proton that accompanies the generation of high-valent metal (–oxo) species *via* O–O bond cleavage. More research focused on this proton is needed.



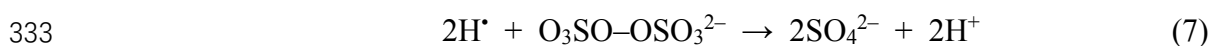
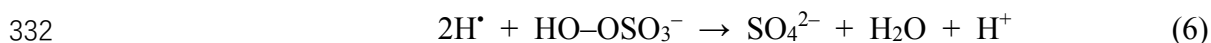
Previous studies concerning the formation of high-valent metal (–oxo) species at

solid-water interfaces did not identify PT (2,25,45). A possible explanation is that reactions mediated by coupled protons tend to be unnoticed because they are ubiquitous. In contrast, the thermochemistry [i.e., energy difference between bonds broken and formed that affects reaction equilibria, typically described using a “square scheme” (Fig. S24) (12,14)] implies that ET and PT are thermodynamically coupled to ensure charge equilibrium (12,18,44). Accordingly, the coupled movement of proton charges compensates for the transferred electrons. The mechanism may be either a concerted PCET [where the  $H^+$  and  $e^-$  are transferred in the same kinetic step (46)], a separate but coupled pathway [PT precedes ET (PTET)], or ET followed by PT (ETPT) (32). We propose that the formation of a high-valent metal (–oxo) species involves a net PCET, thus comprising an inextricably coupled transfer of  $e^-$  and  $H^+$ . Qualitative experimental support for this hypothesis is provided by the model CuO-activated PMS reaction, which is associated with a pH reduction indicating a loss of  $H^+$  to solution (Fig. S25). However, quantitative verification has been lacking, partly due to the difficulty associated with determining the  $H^+/e^-$  stoichiometry  $m/n$  [an integer ratio according to Dalton’s law (Eq. 4)]. Because the bond dissociation free energy (BDFE) of X–H (Eq. 5) is the “gold standard” thermochemical descriptor of I-PCET (12,18,44), it is reasonable to speculate that tight  $H^+/e^-$  coupling involves cleavage of the surface-H bond, increasing  $pK_a$  ( $pK_a = -\log K_a$ , where  $K_a$  is the acid dissociation constant) at the surfaces of metal oxides and yielding high-valent metal (–oxo) species upon electron removal (Fig. 1B and 3B). This speculation assumes that  $H^+$  generation upon dissociation of the surface-H bond will be stoichiometric, accompanied by ET. Consequently, trapping and quantification of coupled protons (dissociated  $H^+$ ) could directly yield to the critical  $m/n$  stoichiometry governing formation of high-valent metal (–oxo) species, enabling a comprehensive understanding of I-PCET. Thus, we present stoichiometric- $H^+$  experimental measurements obtained *via* appropriate, liquid-phase acid–base titrations (Note S12). We quantify dissociated- $H^+$  levels by determining changes in total surface-hydroxyl density (47,48).





The need for equivalent protons can be represented by ascertaining dissociative  $\text{H}^+$  behavior in a model of  $\text{MO}_x$ -mediated O–O bond activation/I-PCET half-reaction (Figs. 1B and 3B). In the presence of 0.1 mM  $\text{HO-OSO}_3^-$  and excess benchmark  $\text{MO}_x$  (2.0 g  $\text{L}^{-1}$   $\text{CuO}$ ) (Note S13), the overall dissociated- $\text{H}^+$  concentration was 0.093 mM, implying a  $\text{H}^+/\text{e}^-$  molar ratio of 1:2 attributable to O–O bond cleavage along with  $2\text{-e}^-$  transfer (Figs. 3C, S26 and Table S3). This result conflicts with the predicted 1:1  $\text{H}^+/\text{e}^-$  stoichiometry of  $\text{Cu}^{\text{III}}$  formation (12,18,44). Furthermore, an identical but  $\text{O}_2$ -free reaction yielded a similar result (Fig. S27 and Table S3). The contradictory outcomes are attributable to the presence of  $\text{H}^+$  acceptors in  $\text{HO-OSO}_3^-$  (Eqs. 2 and 6);  $\text{H}^+$  transferred to the product- $\text{H}_2\text{O}$  cannot be determined *via* titration. If this hypothesis is correct, replacement of  $\text{HO-OSO}_3^-$  with  $\text{O}_3\text{SO-OSO}_3^{2-}$  *via*  $\text{H}^+$ -acceptor site-directed mutagenesis might yield a stoichiometrically compatible  $\text{H}^+$  level (Eqs. 2 and 7). As anticipated, the ratio of transferred  $\text{e}^-$  to coupled  $\text{H}^+$  was 1:1 (Figs. 3D, S28, S29 and Table S3), confirming the existence of a rigorous solid-water interface PCET in which the O–H bond is directly involved (Fig. 3B). To confirm that this I-PCET was not unusual, we extended the range of high-valent metal (–oxo) species from a form that is typically unstable, thus  $\text{Cu}^{\text{III}}$  (49) (as previously described), to stable complexes ( $\text{Ni}^{\text{IV}}=\text{O}$  and  $\text{Co}^{\text{IV}}=\text{O}$ ) (49) and measured the  $\text{H}^+/\text{e}^-$  ratios of transition-metal-oxide ( $\text{NiO}$  and  $\text{Co}_3\text{O}_4$ )-mediated O–O bond activations. As expected, 2-coupled  $\text{H}^+$  was involved in  $\text{Ni}^{\text{IV}}=\text{O}$  and  $\text{Co}^{\text{IV}}=\text{O}$  formation, linked to  $2\text{-e}^-$  transfer (Figs. 3E–H, S30–S37 and Table S3). The  $\text{H}^+/\text{e}^-$  stoichiometry is 1:1, evincing the generality of this I-PCET mechanism.



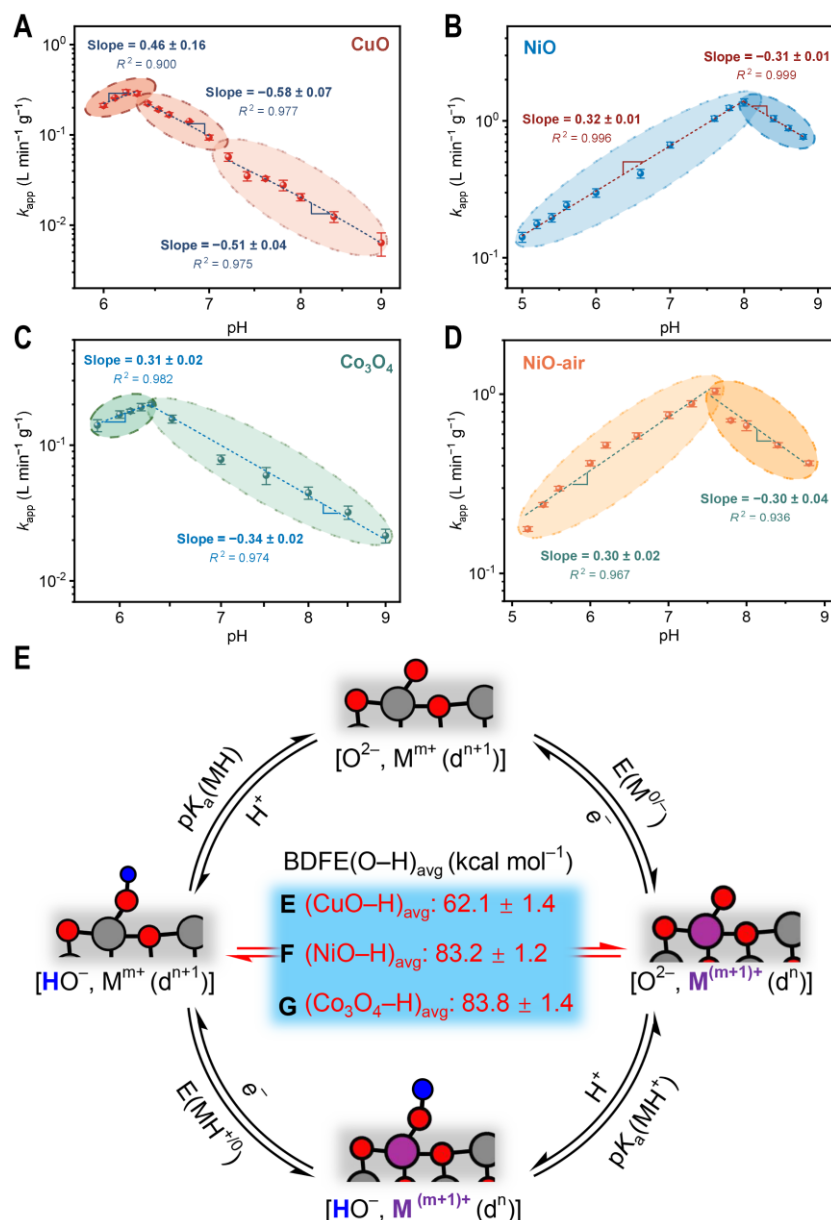


**Fig. 4. Thermokinetic analyses and thermochemical frameworks for interfacial PCET.** Linear correlations were observed between the logarithm of the  $k_{app}$  value and pH, with different slopes for the following systems: (A) CuO/PMS, (B) NiO/PMS, (C) NiO-air/PMS, and (D) Co<sub>3</sub>O<sub>4</sub>/PMS. Experimental conditions: [PMS] = 0.3 mM, [PhOH] = 0.15 mM, catalyst = 0.2 g L<sup>-1</sup>, T = 25 ± 2 °C, 0.2 M borate or glycine buffer. The thermochemical frameworks for (E) CuO, (F) NiO, and (G) Co<sub>3</sub>O<sub>4</sub> are presented, focusing on the BDFE as the primary energetic parameter.

### Thermokinetic analysis

A comprehensive understanding of I-PCET requires kinetic and thermodynamic details. Our initial objective was to gain kinetic insights into the pH-dependent solid-water interface-hosted CPET mechanism. This involves the almost stoichiometric

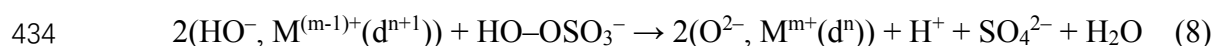


formation of  $\text{PhO}^\bullet$  and high-valent metal (–oxo) species (Note S14), which is relevant in the model CuO-activated PMS context. The duplicated  $k_{\text{app}}$  values are plotted as a function of pH in Figure 1F, which reveals the dependence on proton activity. This dependence is confirmed by the fact that  $\log(k_{\text{app}})$  (approximately) scales with the Brønsted slope or the Brønsted  $\alpha$  with the pH. The  $\alpha$  predicted by Marcus theory is approximately 1/2 under the low driving force of a free energy barrier (18,32) (Fig. 4A and Note S15). It is imperative to emphasize that the Brønsted  $\alpha$ , which establishes a linear correlation between the logarithm of the CPET rate constant [ $\log(k_{\text{CPET}})$ ] and the logarithm of the equilibrium constant [ $\log(k_{\text{eq}})$ ] or the scaled driving force ( $|\Delta G^\circ_{\text{CPET}}|$ ) (50), would provide an invaluable insight into the sensitivities of reaction barriers (rates) to changes in free energy (i.e., the driving force) during rate-limiting I-PCET. Figure 4A shows that as the pH increases from 6.0,  $k_{\text{app}}$  rises in a log-linear manner up to pH 6.2, with a slope of  $0.46 \pm 0.16 \log(\text{L min}^{-1} \text{ g}^{-1}) \text{ pH}^{-1}$ ; after pH 6.2,  $k_{\text{app}}$  decreases with a slope of  $-0.58 \pm 0.07 \log(\text{L min}^{-1} \text{ g}^{-1}) \text{ pH}^{-1}$  up to pH 7.0; and the slope finally becomes  $-0.51 \pm 0.04 \log(\text{L min}^{-1} \text{ g}^{-1}) \text{ pH}^{-1}$  from pH 7.2 to 9.0. Indeed, the initial fractional slope of  $\log(k_{\text{app}}) \text{ pH}^{-1}$  ( $0.46 \pm 0.16$ ) is consistent with an approximately  $\alpha$ -1/2 scaling, as predicted by Marcus theory (18,32). This slope suggests that the relationship between  $\log(k_{\text{app}})$  and pH is analogous to the plot of  $\log(k_{\text{CPET}})$  versus  $\log(k_{\text{eq}})$  or the plot of the barrier force versus the CPET driving force,  $\Delta G^\ddagger$  versus  $|\Delta G^\circ_{\text{CPET}}|$ . These relationships highlight the pivotal role of PT, which agrees with the proposed I-CPET mechanism (14,18,32,51). Moreover,  $\log(k_{\text{app}}) \text{ pH}^{-1}$  scaling, largely independent of buffer concentration (Fig. S38), provides further support for the I-PCET mechanism because it is not perturbed by solvent. However, the electron-only or proton-only pathway is medium-dependent, and charges move (52). Note that the Brønsted slope exhibits an apparently negative  $\alpha$ -scaling based on pH [ $-0.58 \pm 0.07$  and  $-0.51 \pm 0.04 \log(k_{\text{app}}) \text{ pH}^{-1}$ ] (Fig. 4A) across the extensive pH range of 6.2 to 9.0. The reason for this negative  $\alpha$ -scaling is unclear, and further investigations are required.

In the widely accepted CPET mechanism, BDFE constitutes the central energetic parameter (12,18,32). We thus hypothesized that a change in  $\Delta G^\circ_{\text{PT}}$  (the free energy for

PT) according to pH would exhibit a strong correlation with the abovementioned, complex pH dependence. The negative  $\alpha$ -scaling of  $\log(k_{\text{app}}) \text{pH}^{-1}$  reflects the fact that  $\Delta G^\circ_{\text{PT}}$  determines PT- $k_{\text{eq}}$  (12,32); moreover,  $\Delta G^\circ_{\text{ET}}$  (the free energy for ET) is in close balance with  $\Delta G^\circ_{\text{PT}}$  to maintain a remarkably constant BDFE (18). This constant BDFE indicates that the dependence of  $\Delta G^\circ_{\text{PT}}$  on pH (53) enables  $\Delta G^\circ_{\text{PT}}$  to be tuned via regulation of the acidity and basicity of proton donors and acceptors, respectively. The free energy relationship lends further support to the notion that the rate would exhibit distinct responses to alterations in both  $\Delta G^\circ_{\text{PT}}$  and  $\Delta G^\circ_{\text{ET}}$ . This notion can be adequately described using Marcus-type formulations (54,55). Specifically, if  $\Delta G^\circ_{\text{PT}}$  increases when  $\Delta G^\circ_{\text{ET}}$  is already large,  $\Delta G^\circ_{\text{CPET}}$  may approach the intrinsic barrier ( $\lambda$ ) of the CPET, resulting in a rate that is near the peak of the Marcus parabola (32,56). Note also that the irregular dependence of  $k_{\text{app}}$  on pH, combined with the pH-varying  $\Delta G^\circ_{\text{PT}}$ , indicates changes in the base and oxidant strengths ( $\Delta G^\circ_{\text{PT}}$  and  $\Delta G^\circ_{\text{ET}}$ ). Considering the structural diversity of the Cu-site, and the redox evolution of the site during the catalytic cycle (Figs. 1B and 3B), it is unsurprising that  $\Delta G^\circ_{\text{PT}}$  and  $\Delta G^\circ_{\text{ET}}$  vary, consistent with the fact that the valence state of the Cu-site switches between  $\text{Cu}^{\text{II}}$  and  $\text{Cu}^{\text{III}}$ , thereby explaining the variations in  $\Delta G^\circ_{\text{CPET}}$  caused by changes in both  $\Delta G^\circ_{\text{PT}}$  and  $\Delta G^\circ_{\text{ET}}$ . These variations are attributable to differences in base and oxidant strengths of the Cu-site. In particular,  $\text{Cu}^{\text{II}}$  and  $\text{Cu}^{\text{III}}$ , which are Lewis acids, vary based on protonation and deprotonation interactions;  $\Delta G^\circ_{\text{PT}}$  disproportionally influences  $k_{\text{app}}$ . Because  $\text{p}K_{\text{a}}$  serves as an index of proton-donating ability, substantial changes in the Cu-site  $\text{p}K_{\text{a}}$  during oxidation of  $\text{Cu}^{\text{II}}$  to  $\text{Cu}^{\text{III}}$  would modify the relative contributions of  $\Delta G^\circ_{\text{PT}}$  and  $\Delta G^\circ_{\text{ET}}$  to  $\Delta G^\circ_{\text{CPET}}$ . The linear  $\Delta G^\circ_{\text{CPET}}$  could become non-monotonic with respect to pH, based on the co-existence of  $\text{Cu}^{\text{II}}$  and  $\text{Cu}^{\text{III}}$ . Indeed, simultaneous deprotonation of  $\text{Cu}^{\text{II}}$  and  $\text{Cu}^{\text{III}}$  is promoted at high pH ( $\geq 6.2$ ). The titrated  $\text{p}K_{\text{a}}$  of  $\text{Cu}^{\text{II}}$  is  $6.45 \pm 0.31$  (Fig. S39); the  $\text{p}K_{\text{a}}$  of  $\text{Cu}^{\text{III}}$  is presumably less than 7.0 (Note S16). These disparate  $\text{p}K_{\text{a}}$  values result in two very distinct effects on the  $\Delta G^\circ_{\text{PT}}$ , influencing the  $\text{Cu}^{\text{II}}$ -to- $\text{Cu}^{\text{III}}$  PT responsible for formation of high-valent metal (–oxo) species ( $\Delta G^\circ_{\text{PT1}}$ ) (Eq. 8, Figs. 1B and 3B), and on the  $\text{Cu}^{\text{III}}$ -to- $\text{Cu}^{\text{II}}$  PT, triggering  $\text{PhOH}$ -to- $\text{PhO}^\bullet$  oxidation ( $\Delta G^\circ_{\text{PT2}}$ ) (Eq. 3, Figs. 1A and 3A). Thus, in contrast to  $\Delta G^\circ_{\text{PT1}}$ , which

chemically favors a pH increase (from 6.0 to 7.0) (Fig. S39 and Note S17),  $\Delta G^\circ_{\text{PT2}}$  is chemically unfavorable within the same pH region (Fig. S40). The contributions of  $\Delta G^\circ_{\text{PT1}}$  and  $\Delta G^\circ_{\text{PT2}}$  to  $\text{PT-}k_{\text{eq}}$  are combined when determining  $\Delta G^\circ_{\text{PT}}$ ; these combined contributions explain the negative  $\alpha$ -scaling  $\log(k_{\text{app}}) \text{ pH}^{-1}$  correlation. Thus,  $\Delta G^\circ_{\text{PT}}$ , rather than pH, controls the kinetics;  $\Delta G^\circ_{\text{PT}}$  declines as the pH increases from 6.2 to 9.0. The linear correlation between  $k_{\text{app}}$  and  $\Delta G^\circ_{\text{PT}}$  is a defining characteristic of an I-PCET reaction. Next, we considered the BDFE, which is conceptually analogous to the free energy sums of  $\text{p}K_{\text{a}}$  and  $E^\circ$  (the equilibrium potential at the standard state of proton activity, pH 0) plus the  $\Delta G^\circ$  for  $\text{H}^+ + e^- \rightarrow \text{H}^\bullet (C_{\text{G}})$  (12). We thus explored  $k_{\text{app}}$  behavior very close to the CuO  $\text{p}K_{\text{a}}$  because if the surface Brønsted-basic site (i.e., surface hydroxides near  $\text{Cu}^{\text{II}}$ ) served as a proton donor, PT would be exquisitely sensitive to  $\text{p}K_{\text{a}}$  and the inflection point of the volcano-shaped activity profile would (approximately) equal the  $\text{p}K_{\text{a}}$  (12). As anticipated, the experimental  $\text{p}K_{\text{a}}$  was  $6.45 \pm 0.31$  (Fig. S39), indicating that the surface Brønsted-basic hydroxide site (also termed the Lewis-acid site redox-linked PT component) participated in PCET in a manner analogous to that of enzyme-catalyzed reactions (57). This finding confirmed that PT plays a pivotal role in the kinetics. The  $\text{Cu}^{\text{III}}$ -to- $\text{Cu}^{\text{II}}$  PT is the reverse of the above steps (Figs. 1A, 3A and Eq. 3). At higher pH values ( $\geq 6.2$ ), unfavorable protonation of  $\text{Cu}^{\text{III}}$  inhibits PT from PhOH (corresponding to PhOH-to- $\text{PhO}^\bullet$ ) (Fig. S40). Thus, re-reduction of  $\text{Cu}^{\text{III}}$  is regulated by PT. Note that calculation of  $\Delta G^\circ_{\text{PT}}$  is not yet feasible; the structure and energetics of the transition-state  $\text{Cu}^{\text{III}}$  remain unknown. Consequently, it is not possible to build a rigorous mechanistic model that accurately predicts kinetic trends. However, the primary I-PCET thermochemical parameter (i.e., the BDFE that dictates PCET reactivity) can be investigated *via* slow scan-rate cyclic voltammetry (CV) (58) (Fig. S41). The quasi-reversible  $E^{\text{eq}}$  plotted as a function of the applied pH yielded an intercept  $E^\circ$  value of  $0.405 \pm 0.04$  V versus a standard hydrogen electrode (SHE) at pH 0; the  $E^\circ$  was then converted to a BDFE of  $62.1 \pm 1.4$  kcal mol<sup>-1</sup> using a more general form of thermochemical cycling (18) (see Note S18 for details) (Fig. 4E). Together, these outcomes substantiate the fact that PT is coupled with ET *via* redox Cu-sites, emphasizing the mechanistic attributes of I-PCET.



435 The thermodynamic analyses were further extended to  $\text{Ni}^{\text{IV}}=\text{O}$  and  $\text{Co}^{\text{IV}}=\text{O}$  to  
 436 emphasize the generality of I-PCET. The volcano-shaped  $k_{\text{app}}$  profiles versus pH (Figs.  
 437 1G and 1H) were fitted to extract the log-linear dependence of  $k_{\text{app}}$  on pH and  
 438  $\log(k_{\text{app}}) \text{pH}^{-1}$  slopes. The values for  $\text{Ni}^{\text{IV}}=\text{O}$  are  $0.32 \pm 0.01$  (pH 5.0 to 8.0) and  $-0.31$   
 439  $\pm 0.10$  (pH 8.0 to 8.8); for  $\text{Co}^{\text{IV}}=\text{O}$ , these values are  $0.31 \pm 0.02$  (pH 5.8 to 6.3) and  $-$   
 440  $0.34 \pm 0.02$  (pH 6.3 to 9.0) (Figs. 4B and 4C). Notably, the Brønsted  $\alpha$  values were  
 441 considerably smaller than the anticipated 1/2 (18,32), indicating that  $\Delta G^\circ_{\text{CPET}}$   
 442 substantially increases and then gradually approaches the CPET  $\lambda$  predicted by Marcus  
 443 theory (18). However, the interpretation of such shallow slopes is unclear, although  
 444 several recent rate/driving force studies of PCET also showed very small  $\alpha$ -values (59–  
 445 61). The Bernasconi principle of non-perfect synchronization (NPS) (62) assumes that  
 446 fundamental reactions involving multiple concurrent processes (e.g., electron  
 447 localization/delocalization and bonding/cleavage) may proceed *via* “unbalanced” or  
 448 “asynchronous” transition states (62–64). We thus suggest that the transition state of I-  
 449 PCET involves concerted transfer of  $\text{H}^+$  and  $e^-$ , but in an asynchronous manner. Then,  
 450 a larger  $\alpha$  leads to a more pronounced PT “character” of the transition state and a greater  
 451 sensitivity to changes in PT-driving forces (65,66). Accordingly, the PT characteristics  
 452 of the rate-determining transition states may differ among  $\text{Ni}^{\text{IV}}=\text{O}$ ,  $\text{Co}^{\text{IV}}=\text{O}$ , and  $\text{Cu}^{\text{III}}$ ,  
 453 reflecting variations in CPET synchronicity. The observed variations in  $\alpha$  may indicate  
 454 one- and/or two-electron valence interconversions at Lewis-acid metal sites. These  
 455 include  $\text{Cu}^{\text{III}} \rightleftharpoons \text{Cu}^{\text{II}}$  ( $1-e^-$ ),  $\text{Co}^{\text{IV}}=\text{O} \rightleftharpoons \text{Co}^{\text{III}}/\text{Co}^{\text{II}}$  ( $1-$  and  $2-e^-$ ), and  $\text{Ni}^{\text{IV}}=\text{O} \rightleftharpoons \text{Ni}^{\text{II}}$  ( $2-e^-$ )  
 456 (switchable electronic states, or “redox isomers”), as well as Lewis-acid metal site-  
 457 dependent valence tautomerism (67) (with lesser ETs and relatively greater PTs leading  
 458 to increased  $\alpha$  values; for example,  $\text{Cu}^{\text{III}} \rightleftharpoons \text{Cu}^{\text{II}}$  associated with more complete PT  
 459 during CPET compared with  $\text{Co}^{\text{IV}}=\text{O} \rightleftharpoons \text{Co}^{\text{III}}/\text{Co}^{\text{II}}$  and  $\text{Ni}^{\text{IV}}=\text{O} \rightleftharpoons \text{Ni}^{\text{II}}$ ). In contrast to  
 460  $\text{Cu}^{\text{III}}$ , the volcano-shaped activity inflection point for  $\text{Ni}^{\text{IV}}=\text{O}$  occurs at pH 8.0 (Fig. 4B),  
 461 which considerably differs from the  $\text{pK}_\text{a}$  values of NiO ( $\text{pK}_{\text{a1}} = 4.29 \pm 0.32$ ,  $\text{pK}_{\text{a2}} = 9.10$   
 462  $\pm 0.22$ ) (Fig. S42). Notably, the  $\text{Ni}^{\text{IV}}=\text{O}$  inflection point is very close to  $\text{pH}_{\text{pzc}}$  ( $\text{pH}_{\text{pzc}} =$

8.15 ± 0.05 according to quantitative titration) (Fig. S42); this similarity has not been previously reported. To illustrate the importance of the inflection point at pH<sub>pzc</sub>, the surface Brønsted acid–base characteristics of the model catalyst NiO were manipulated to obtain NiO-air (Figs. S43, S44 and Note S19), and a strikingly analogous outcome was observed (Fig. 4D). The pH<sub>pzc</sub> (7.55 ± 0.03 of NiO-air according to quantitative titration) affected the activity-inflection point pH (7.6) (Figs. 4D, S43, and S44)). The pH<sub>pzc</sub> also predicted the activity-inflection point pH of another model catalyst, Co<sub>3</sub>O<sub>4</sub> (Fig. S45). One possible explanation is that high-valent metal species require electronically stable oxygenic ligands (Ni<sup>IV</sup>=O and Co<sup>IV</sup>=O), rather than less stable metal–oxo species (Cu<sup>III</sup>) (49). Alternatively, the electrostatic effects of a double-layer charge structure may be involved. A deviation from the pH<sub>pzc</sub> pH triggered double-layer reorganization and thus shifts in ΔG°<sub>CPET</sub> (68). Moreover, the BDFE values of NiO and Co<sub>3</sub>O<sub>4</sub> were calculated to be 83.2 ± 1.2 and 83.8 ± 1.4 kcal mol<sup>−1</sup>, respectively (Figs. 4E, S46 and S47), thereby emphasizing the explicit dependence on PT.

To enhance the overall understanding of I-PCET *via* transition metal-mediated O–O bond activation, we now summarize the principal mechanistic features that distinguish I-PCET from well-studied reactions such as electrocatalytic PCET (E-PCET) (Note S20), with a primary focus on proton activity (pH), particularly at the solid-liquid interface. One difference is the noncovalent, inner-sphere hydrogen-bonding interaction (Fig. S48); the hydrogen bonding strength between a protic PMS-oxidant and a metal site limits the proton tunnelling rate, thus affecting the generation of high-valent metal (–oxo) species. Furthermore, the I-PCET mechanism is based on the kinetic dependencies of the surface Brønsted acid–base parameters, particularly pK<sub>a</sub> and pH<sub>pzc</sub>. This relationship is primarily attributable to changes in free energy, which greatly affect *k*<sub>eq</sub>. Additionally, in contrast to the electrified interface of E-PCET, where an aqueous electrochemical double layer controls the kinetics and thermodynamics of both PT and ET (69), the solvation interface hosts the chemical potentials of protons and electrons; the potentials are tuned according to the redox potentials of the metal centers (Cu<sup>III</sup>, Ni<sup>IV</sup>=O, and Co<sup>IV</sup>=O), thus favoring I-PCET. Finally, I-PCET is defined

by concerted but asynchronous PT and ET. The difference in synchronicity of CPET is attributable to the valence tautomerism of the metal center.

To further extend polymerizations mediated by persulfate-based oxidation, we examined another typical aromatic, aniline. As expected, PT created organic radicals, followed by crosslinked and polymerization products (Fig. S49). These data illustrate the broad range of organic contaminants that can be polymerized.

## Conclusions

This study highlights the pivotal roles of coupled protons in redox reaction activities at the solid-water interfaces of various persulfate-based, oxidative polymerization model systems. Further research is required to derive a thermochemical model that fully describes the relationship between the reaction rate and the driving force, particularly with respect to how coupled electrons and protons (i.e., net PCET) proceed across a solid-solution interface. Our findings suggest that reaction rates can be increased by modifying the force that drives interfacial PT through pH alteration during the overall PCET reaction. The data also indicate that the principal parameters of benchmark  $\text{MO}_x$ -based catalysts, namely the Lewis acid/base (electron withdrawing/donating) potentials and Brønsted acid/base (proton donor/acceptor) characteristics, govern I-PCET. This enables rational catalyst design.

Careful acid–base titration analyses revealed a 1:1 proton:electron stoichiometry regarding the key fundamental components (PT and ET) of interfacial redox reactions. There are two coupled redox half-reactions, comprising the CPETs of  $\text{Cu}^{\text{II}}$ -to- $\text{Cu}^{\text{III}}$  and  $\text{Cu}^{\text{III}}$ -to- $\text{Cu}^{\text{II}}$ . The former reaction forms high-valent metal (–oxo) species, whereas the latter reaction oxidizes  $\text{PhOH}$  to  $\text{PhO}^\bullet$ .  $\text{MO}_x$ -mediated O–O bond activation proceeds *via* interfacial ET coupled to proton movement within a solvent. These findings greatly improve the overall understanding of interfacial redox activity. Proton and electron coupling determine the reaction rate. Such coupling removes the need for high-energy chemical intermediates (18) and is thermodynamically favorable. We suggest that other



reactions also are significantly affected by the previously underappreciated reaction parameter of proton activity.

## References and Notes

1. W. B. Li, R. D. Tang, S. Xiong, L. Li, Z. P. Zhou, L. Su, D. X. Gong, Y. C. Deng, High-valent metal-oxo species in catalytic oxidations for environmental remediation and energy conversion. *Coord. Chem. Rev.* **510**, 215840 (2024).
2. H. Z. Liu, X. X. Shu, M. J. Huang, B. B. Wu, J. J. Chen, X. S. Wang, H. L. Li, H. Q. Yu, Tailoring *d*-band center of high-valent metal-oxo species for pollutant removal *via* complete polymerization. *Nat. Commun.* **15**, 2327 (2014).
3. X. Zhang, J. J. Tang, L. L. Wang, C. Wang, L. Chen, X. Q. Chen, J. S. Qian, B. C. Pan, Nanoconfinement-triggered oligomerization pathway for efficient removal of phenolic pollutants *via* a Fenton-like reaction. *Nat. Commun.* **15**, 917 (2014).
4. S. J. Zhang, H. C. Zheng, P. G. Tratnyek, Advanced redox processes for sustainable water treatment. *Nat. Water.* **1**, 666–681 (2023).
5. X. P. Zhang, A. Chandra, Y. M. Lee, R. Cao, K. Ray, W. Nam, Transition metal-mediated O–O bond formation and activation in chemistry and biology. *Chem. Soc. Rev.* **50**, 4804–4811 (2021).
6. M. Guo, Y. M. Lee, S. Fukuzumi, W. Nam, Biomimetic metal-oxidant adducts as active oxidants in oxidation reactions. *Coord. Chem. Rev.* **435**, 213807 (2021).
7. S. Fukuzumi, K. B. Cho, Y. M. Lee, S. Hong, W. Nam, Mechanistic dichotomies in redox reactions of mononuclear metal–oxygen intermediates. *Chem. Soc. Rev.* **49**, 8988–9027 (2020).
8. W. J. Zhu, S. M. Jang, J. Xiong, R. Ezhov, X. X. Li, T. Kim, M. S. Seo, Y. M. Lee, Y. Pushkar, R. Sarangi, Y. Guo, W. Nam, A mononuclear non-heme iron(III)–peroxo complex with an unprecedented high O–O stretch and electrophilic reactivity. *J. Am. Chem. Soc.* **143**, 15556–15561 (2021).
9. G. L. Tripodi, M. M. J. Dekker, J. Roithová, L. Q. Jr, Tuning the H-atom transfer reactivity of iron(IV)-oxo complexes as probed by infrared photodissociation spectroscopy. *Angew. Chem. Int. Ed.* **60**, 7126–7131 (2021).
10. A. Vasilopoulos, S. W. Krska, S. S. Stahl, C(sp<sup>3</sup>)-H methylation enabled by peroxide photosensitization and Ni-mediated radical coupling. *Science* **372**, 398–403 (2021).
11. B. C. Hodges, E. L. Cates, J. H. Kim, Challenges and prospects of advanced oxidation water treatment processes using catalytic nanomaterials. *Nat. Nanotechnol.* **13**, 642–650 (2018).
12. J. M. Mayer, Bonds over Electrons: Proton coupled electron transfer at solid–solution interfaces. *J. Am. Chem. Soc.* **145**, 7050–7064 (2023).

- 556 13. J. N. Schrauben, R. Hayoun, C. N. Valdez, M. Braten, L. Fridley, J. M. Mayer,  
557 Titanium and zinc oxide nanoparticles are proton-coupled electron transfer agents.  
558 *Science* **336**, 1298–1301 (2012).
- 559 14. R. E. Warburton, A. V. Soudackov, S. Hammes-Schiffer, Theoretical modeling of  
560 electrochemical proton-coupled electron transfer. *Chem. Rev.* **122**, 10599–10650  
561 (2022).
- 562 15. B. P. Rimgard, Z. Tao, G. A. Parada, L. F. Cotter, S. Hammes-Schiffer, J. M. Mayer,  
563 L. Hammarstrom, Proton-coupled energy transfer in molecular triads. *Science* **377**,  
564 742–747 (2022).
- 565 16. G. A. Parada, Z. K. Goldsmith, S. Kolmar, B. Pettersson Rimgard, B. Q. Mercado,  
566 L. Hammarström, S. Hammes-Schiffer, J. M. Mayer, Concerted proton-electron  
567 transfer reactions in the Marcus inverted region. *Science* **364**, 471–475 (2019).
- 568 17. K. S. Westendorff, M. J. Hülsey, T. S. Wesley, Y. Román-Leshkov, Y. Surendranath,  
569 Electrically driven proton transfer promotes Brønsted acid catalysis by orders of  
570 magnitude. *Science* **383**, 757–763 (2024).
- 571 18. R. G. Agarwal, S. C. Coste, B. D. Groff, A. M. Heuer, H. Noh, G. A. Parada, C. F.  
572 Wise, E. M. Nichols, J. J. Warren, J. M. Mayer, Free energies of proton-coupled  
573 electron transfer reagents and their applications. *Chem. Rev.* **122**, 1–49 (2022).
- 574 19. Z. W. She, J. Kibsgaard, C. F. Dickens, I. Chorkendorff, J. K. Norskov, T. F.  
575 Jaramillo, Combining theory and experiment in electrocatalysis: Insights into  
576 materials design. *Science* **355**, eaad4998 (2017).
- 577 20. S. W. Boettcher, Y. Surendranath, Heterogeneous electrocatalysis goes chemical.  
578 *Nat. Catal.* **4**, 4–5 (2021).
- 579 21. H. N. Nong, L. J. Falling, A. Bergmann, M. Klingenhof, H. P. Tran, C. Spöri, R.  
580 Mom, J. Timoshenko, G. Zichittella, A. Knop-Gericke, S. Piccinin, J. Pérez-  
581 Ramírez, B. R. Cuenya, R. Schlögl, P. Strasser, D. Teschner, T. E. Jones, Key role  
582 of chemistry versus bias in electrocatalytic oxygen evolution. *Nature* **587**, 408–413  
583 (2020).
- 584 22. D. P. Zhang, Y. X. Li, P. F. Wang, J. Y. Qu, Y. Li, S. H. Zhan, Dynamic active-site  
585 induced by host-guest interactions boost the Fenton-like reaction for organic  
586 wastewater treatment. *Nat. Commun.* **14**, 3538 (2023).
- 587 23. Z. Y. Guo, Y. Si, W. Q. Xia, F. Wang, H. Q. Liu, C. Yang, W. J. Zhang, W. W. Li,  
588 Electron delocalization triggers nonradical Fenton-like catalysis over spinel oxides.  
589 *Proc. Natl. Acad. Sci.* **119**, e2201607119 (2022).
- 590 24. Z. Y. Guo, R. Sun, Z. Huang, X. Han, H. Wang, C. Chen, Y. Q. Liu, X. Zheng, W.  
591 Zhang, X. Hong, W. W. Li, Crystallinity engineering for overcoming the activity-  
592 stability tradeoff of spinel oxide in Fenton-like catalysis. *Proc. Natl. Acad. Sci.* **120**,  
593 e2220608120 (2023).
- 594 25. M. Huang, Y. S. Li, C. Q. Zhang, C. Cui, Q. Q. Huang, M. Li, Z. Qiang, T. Zhou,  
595 X. Wu, H. Q. Yu, Facilely tuning the intrinsic catalytic sites of the spinel oxide for

- 596 peroxymonosulfate activation: From fundamental investigation to pilot-scale  
597 demonstration. *Proc. Natl. Acad. Sci.* **119**, e2202682119 (2022).
- 598 26. Y. J. Zhang, G. X. Huang, L. R. Winter, J. J. Chen, L. Tian, S. C. Mei, Z. Zhang, F.  
599 Chen, Z. Y. Guo, R. Ji, Y. Z. You, W. W. Li, X. W. Liu, H. Q. Yu, M. Elimelech,  
600 Simultaneous nanocatalytic surface activation of pollutants and oxidants for highly  
601 efficient water decontamination. *Nat. Commun.* **13**, 3005 (2022).
- 602 27. L. D. Liu, Q. Liu, Y. Wang, J. Huang, W. J. Wang, L. Duan, X. Yang, X. Y. Yu, X.  
603 Han, N. Liu, Nonradical activation of peroxydisulfate promoted by oxygen  
604 vacancy-laden NiO for catalytic phenol oxidative polymerization. *Appl. Catal., B*  
605 2019, **254**, 166–173 (2019).
- 606 28. X. Gao, Z. C. Yang, W. Zhang, B. C. Pan, Carbon redirection *via* tunable Fenton-  
607 like reactions under nanoconfinement toward sustainable water treatment. *Nat.*  
608 *Commun.* **15**, 2808 (2024).
- 609 29. Y. Q. Yan, Z. S. Wei, X. G. Duan, M. C. Long, R. Spinney, D. D. Dionysiou, R. Y.  
610 Xiao, P. J. J. Alvarez, Merits and limitations of radical vs. nonradical pathways in  
611 persulfate-based advanced oxidation processes. *Environ. Sci. Technol.* **57**, 12153–  
612 12179 (2023).
- 613 30. W. Ren, C. Cheng, P. H. Shao, X. B. Luo, H. Zhang, S. B. Wang, X. G. Duan,  
614 Origins of electron-transfer regime in persulfate-based nonradical oxidation  
615 processes. *Environ. Sci. Technol.* **56**, 78–97 (2021).
- 616 31. M. H. V. Huynh, T. J. Meyer, Proton-coupled electron transfer. *Chem. Rev.* **107**,  
617 5004–5064 (2007).
- 618 32. R. Tyburski, T. Liu, S. D. Glover, L. Hammarström, Proton-coupled electron  
619 transfer guidelines, fair and square. *J. Am. Chem. Soc.* **143**, 560–576 (2021).
- 620 33. N. B. Lewis, R. P. Bisbey, K. S. Westendorff, A. V. Soudackov, Y. Surendranath, A  
621 molecular-level mechanistic framework for interfacial proton-coupled electron  
622 transfer kinetics. *Nat. Chem.* **16**, 343–352 (2024)
- 623 34. Y. Wei, J. Miao, J. X. Ge, J. Y. Lang, C. Y. Yu, L. Z. Zhang, P. J. J. Alvarez, M.  
624 Long, Ultrahigh peroxymonosulfate utilization efficiency over CuO nanosheets via  
625 heterogeneous Cu (III) formation and preferential electron transfer during  
626 degradation of phenols. *Environ. Sci. Technol.* **56**, 8984–8992 (2022).
- 627 35. M. K. Zhang, W. Chen, M. L. Xu, Z. Wei, D. Zhou, J. Cai, Y. X. Chen, How buffers  
628 resist electrochemical reaction-induced pH shift under a rotating disk electrode  
629 configuration. *Anal. Chem.* **93**, 1976–1983 (2021).
- 630 36. V. I. Parvulescu, F. Epron, H. Garcia, P. Granger, Recent progress and prospects in  
631 catalytic water treatment. *Chem. Rev.* **122**, 2981–3121 (2021).
- 632 37. W. Ren, Q. M. Zhang, C. Cheng, F. Miao, H. Zhang, X. B. Luo, S. B. Wang, X. G.  
633 Duan, Electro-induced carbon nanotube discrete electrodes for sustainable  
634 persulfate activation. *Environ. Sci. Technol.* **56**, 14019–14029 (2022).

- 635 38. Y. Jing, B. P. Chaplin, Mechanistic study of the validity of using hydroxyl radical  
636 probes to characterize electrochemical advanced oxidation processes. *Environ. Sci.*  
637 *Technol.* **51**, 2355–2365 (2017).
- 638 39. T. Zhang, Y. Chen, Y. R. Wang, J. Le Roux, Y. Yang, J. P. Croué, Efficient  
639 peroxydisulfate activation process not relying on sulfate radical generation for  
640 water pollutant degradation. *Environ. Sci. Technol.* **48**, 5868–5875 (2014).
- 641 40. T. S. Chen, H. Y. Dong, Y. H. Yu, J. Chen, J. H. Xu, Y. K. Sun, X. H. Guan, Neutral  
642 phenolic contaminants are not necessarily more resistant to permanganate  
643 oxidation than their dissociated counterparts: Importance of proton-coupled  
644 electron transfer. *Environ. Sci. Technol.* **57**, 17620–17628 (2023).
- 645 41. F. Leresche, L. Ludvíková, D. Heger, U. Gunten, S. Canonica, Quenching of an  
646 aniline radical cation by dissolved organic matter and phenols: A laser flash  
647 photolysis study. *Environ. Sci. Technol.* **54**, 15057–15065 (2020).
- 648 42. L. H. Wang, H. D. Xu, N. Jiang, Z. M. Wang, J. Jiang, T. Zhang, Trace cupric  
649 species triggered decomposition of peroxymonosulfate and degradation of organic  
650 pollutants: Cu(III) being the primary and selective intermediate oxidant. *Environ.*  
651 *Sci. Technol.* **54**, 4686–4694 (2020).
- 652 43. Y. Wang, Y. Wu, Y. Yu, T. Pan, D. T. Li, D. Lambropoulou, X. Yang, Natural  
653 polyphenols enhanced the Cu(II)/peroxymonosulfate (PMS) oxidation: The  
654 contribution of Cu(III) and OH $\cdot$ . *Water Res.* **186**, 116326 (2020).
- 655 44. J. J. Warren, T. A. Tronic, J. M. Mayer, Thermochemistry of proton-coupled  
656 electron transfer reagents and its implications. *Chem. Rev.* **110**, 6961–7001 (2010).
- 657 45. Q. Y. Wu, Z. W. Yang, Z. W. Wang, W. L. Wang, Oxygen doping of cobalt-single-  
658 atom coordination enhances peroxymonosulfate activation and high-valent cobalt-  
659 oxo species formation. *Proc. Natl. Acad. Sci.* **120**, e2219923120 (2023).
- 660 46. J. W. Darcy, B. Koronkiewicz, G. A. Parada, J. M. Mayer, A continuum of proton-  
661 coupled electron transfer reactivity. *Acc. Chem. Res.* **51**, 2391–2399 (2018).
- 662 47. A. Mahdavi-Shakib, T. N. Whittaker, T. Y. Yun, K. B. S. Kumar, L. C. Rich, S.  
663 Wang, R. M. Rioux, L. C. Grabow, B. D. Chandler, The role of surface hydroxyls  
664 in the entropy-driven adsorption and spillover of H $_2$  on Au/TiO $_2$  catalysts. *Nat.*  
665 *Catal.* **6**, 710–719 (2023).
- 666 48. M. Szekeres, E. Tombácz, Surface charge characterization of metal oxides by  
667 potentiometric acid–base titration, revisited theory and experiment. *Colloids Surf.*  
668 *A Physicochem. Eng. Asp.* **414**, 302–313 (2012).
- 669 49. V. A. Larson, B. Battistella, K. Ray, N. Lehnert, W. Nam, Iron and manganese oxo  
670 complexes, oxo wall and beyond. *Nat. Rev. Chem.* **4**, 404–419 (2020).
- 671 50. E. R. Sayfutyarova, Y. C. Lam, S. Hammes-Schiffer, Hammes-Schiffer, Strategies  
672 for enhancing the rate constant of C–H bond cleavage by concerted proton-coupled  
673 electron transfer. *J. Am. Chem. Soc.* **141**, 15183–15189 (2019).

- 674 51. S. Hammes-Schiffer, Proton-coupled electron transfer: Moving together and  
675 charging forward. *J. Am. Chem. Soc.* **137**, 8860–8871 (2015).
- 676 52. H. Noh, J. M. Mayer, Medium-independent hydrogen atom binding isotherms of  
677 nickel oxide electrodes. *Chem* **8**, 3324–3345 (2022).
- 678 53. C. L. Chen, Y. T. Chen, A. P. Demchenko, P. T. Chou, Amino proton donors in  
679 excited-state intramolecular proton-transfer reactions. *Nat. Rev. Chem.* **2**, 131–143  
680 (2018).
- 681 54. T. F. Liu, R. Tyburski, S. H. Wang, R. Fernández-Terán, S. Ott, L. Hammarström,  
682 elucidating proton-coupled electron transfer mechanisms of metal hydrides with  
683 free energy- and pressure-dependent kinetics. *J. Am. Chem. Soc.* **141**, 17245–17259  
684 (2019).
- 685 55. M. Bourrez, R. Steinmetz, S. Ott, F. Gloaguen, L. Hammarström, Concerted  
686 proton-coupled electron transfer from a metal-hydride complex. *Nat. Chem.* **7**,  
687 140–145 (2015).
- 688 56. R. A. Marcus, N. Sutin, Electron transfers in chemistry and biology. *Biochim.*  
689 *Biophys. Acta.* **811**, 265–322 (1985).
- 690 57. K. S. Chen, J. Hirst, R. Camba, C. A. Bonagura, C. D. Stout, B. K. Burgess, F. A.  
691 Armstrong, Atomically defined mechanism for proton transfer to a buried redox  
692 centre in a protein. *Nature* **405**, 265–322 (2000).
- 693 58. Y. Samantaray, D. J. Martin, R. G. Agarwal, N. J. Gibson, J. M. Mayer, Proton-  
694 coupled electron transfer of cerium oxide nanoparticle thin-film electrodes. *J. Phys.*  
695 *Chem. C.* **127**, 4015–4020 (2023).
- 696 59. G. Q. Qiu, R. R. Knowles, Rate-driving force relationships in the multisite proton-  
697 coupled electron transfer activation of ketones. *J. Am. Chem. Soc.* **141**, 2721–2730  
698 (2019).
- 699 60. T. F. Markle, J. W. Marcy, J. M. Mayer, A new strategy to efficiently cleave and  
700 form C–H bonds using proton-coupled electron transfer. *Sci. Adv.* **4**, eaat5776  
701 (2018).
- 702 61. J. W. Darcy, S. S. Kolmar, J. M. Mayer, Transition state asymmetry in C–H bond  
703 cleavage by proton-coupled electron transfer. *J. Am. Chem. Soc.* **141**, 10777–10787  
704 (2019).
- 705 62. C. F. Bernasconi, The principle of imperfect synchronization: I. Ionization of  
706 carbon acids. *Tetrahedron* **41**, 3219–3234 (1985).
- 707 63. C. F. Bernasconi, The principle of nonperfect synchronization: More than a  
708 qualitative concept? *Acc. Chem. Res.* **25**, 9–16 (1992).
- 709 64. D. Bím, M. Maldonado-Domínguez, L. Rulišek, M. Srnec, Beyond the classical  
710 thermodynamic contributions to hydrogen atom abstraction reactivity. *Proc. Natl.*  
711 *Acad. Sci.* **115**, E10287–E10294 (2018).
- 712 65. W. P. Jencks, A primer for the Bema Hapothle. An empirical approach to the

characterization of changing transition-state structures. *Chem. Rev.* **85**, 511–527 (1985).

66. K. Teindl, B. O. Patrick, E. M. Nichols, Linear free energy relationships and transition state analysis of CO<sub>2</sub> reduction catalysts bearing second coordination spheres with tunable acidity. *J. Am. Chem. Soc.* **145**, 17176–17186 (2023).

67. E. D. Raczyńska, W. Kosińska, B. Ośmiałowski, R. Gawinecki, Tautomeric equilibria in relation to pi-electron delocalization. *Chem. Rev.* **105**, 3561–3612 (2005).

68. P. Li, Y. L. Jiang, Y. C. Hu, Y. N. Men, Y. W. Liu, W. B. Cai, S. L. Chen, Hydrogen bond network connectivity in the electric double layer dominates the kinetic pH effect in hydrogen electrocatalysis on Pt. *Nat. Catal.* **5**, 900–911 (2022).

69. M. W. Swift, J. W. Swift, Y. Qi, Modeling the electrical double layer at solid-state electrochemical interfaces. *Nat. Comput. sci.* **1**, 212–220 (2021).

## Acknowledgements

The authors thank the entirety of the Profs. Zhongbo Zhou, Shiqiang Wei, Dingyong Wang, Luo Peng, Yongmin Wang, and Hong Chen labs for their support throughout this project.

## Funding:

The studies were financially supported by the Natural Science Foundation of Chongqing under grant number CSTB2022NSCQ-MSX0448, by the Sichuan Science and Technology Program under grant number 2023NSFSC0801, and by the Chongqing Municipal Education Commission under grants KJQN202200202 and KJQN202100214.

## Author contributions:

Conceptualization: L.D.L.

Data curation: W.T.L., J.H.C., K.Y.C.

Formal analysis: W.T.L., J.H.C., K.Y.C.

Funding acquisition: L.D.L.

Investigation: W.T.L., J.H.C., K.Y.C., H.J.T., S.A.



742 Methodology: L.D.L., W.T.L.  
743 Project administration: L.D.L.  
744 Resources: L.D.L.  
745 Supervision: L.D.L.  
746 Validation: W.T.L., J.H.C., K.Y.C.  
747 Writing – original draft: L.D.L., W.T.L., J.H.C.  
748 Writing – review & editing: L.D.L.

749 **Competing interests:**

750 The authors declare the following competing financial interests: W.T.L., J.H.C., K.Y.C.,  
751 H.J.T., S.A., and L.D.L are the inventors on the patent application, submitted by  
752 Southwest University, which covers the use of proton activity to modulate the  
753 decontamination activity.

754 **Data and materials availability:**

755 All data are available in the main text or the supplementary materials.  
756